CHAPTER 4

PARABOLIC AND EXPONENTIALLY TAPERING PVEHS UNDER ROTATIONAL MOTION

The design and validation of parabolic and exponentially tapering width PVEHs for rotational motion applications are presented in this chapter. Hamilton's equation is used to develop the electromechanically coupled motion equations. In this case, the kinetic energy due to rotational motion and external workdone due to the resultant centrifugal forces are included in the energy expressions. Galerkin's discretization approach is used to obtain the mass normalized mode shapes. ANSYS Mechanical APDL and experimental methods are used to validate the mathematical models of the two RVEHs. Finally, both RVEHs' numerical, ANSYS simulation, and experimental results are presented and compared.

4.1 Outline

Sensors are used to monitor the health of rotating systems and mechanisms, including turbines and propellers, smart vehicle wheels, fault detection mechanisms, and active-passive vibration isolation of rotating structures. Designing a device to power those low-power sensors by locally harvesting the abundant rotational energy is of great

interest. The piezoelectric potential remains under-utilized due to the inadequate distribution of strain in the host structure, reducing the effectiveness of commonly used rectangular rotational piezoelectric vibration energy harvesters (RVEH). Unlike discussed in Chapter 3, not many researchers have investigated techniques to boost the performance of RVEHs by modifying the cantilever structures. To formulate mathematical models for the RVEH, researchers often consider the OC voltage response or occasionally a simple resistive load. The mathematical modeling used for RVEH systems is simplified and leaves out several critical parameters associated with the rotational motion and piezoelectric energy harvesting. Therefore, it's desired to develop parabolic and exponentially tapering width RVEHs along with a multimodal electromechanical coupled mathematical model with FE and experimental validation to investigate the effects of the characteristic parameters associated with rotational energy harvesting. The harvester is attached with a tip mass to manipulate the harvesters' natural frequencies, and the rotational motion is applied through a rotating shaft.

4.2 Mathematical Modeling

The electromechanically coupled motion equations of the proposed rotational parabolic and exponentially tapering width PVEH with a tip load are formulated using Hamilton's equation and Ohm's law. The line diagram of the proposed tapering width beams is similar to Figure 3.1. The width of the host structure and the PZT patch of the parabolic and exponentially tapering harvester varies as per the relations $b(x) = b_0\left(1-4\sqrt{\phi x}\right)$ and $b(x) = b_0 e^{-\phi x}$, respectively.

4.2.1 Theoretical framework

The proposed composite piezoelectric-coupled tapering width RVEH with a piezoelectric-coupled beam consisting of a PZT patch attached over the central host beam is shown in Figure 4.1. The harvester has one end tied with a weight block to bring down the harvester's resonant frequency for low-frequency applications. The fixed end is at the *Y*-axis, and the system revolves about the Y'-axis, parallel to the *Y*-axis. The Y'-axis is the central axis of the rotating hub, as depicted in Figures 4.1a and 4.1b. The cross-sectional area of the PZT patch and the host beam are $A_p(x)=b(x)t_p$ and $A_h(x)=b(x)t_h$, respectively, at $x'=r+x$. $E_hI_h(x)=\frac{E_h(z_1^3-z_0^3)}{3}b(x)$ and $E_pI_p(x)=\frac{E_p(z_2^3-z_1^3)}{3}b(x)$ are the flexural rigidity at an elemental section. The positions of z_0, z_1, and z_2 are shown in Figure 4.1c.

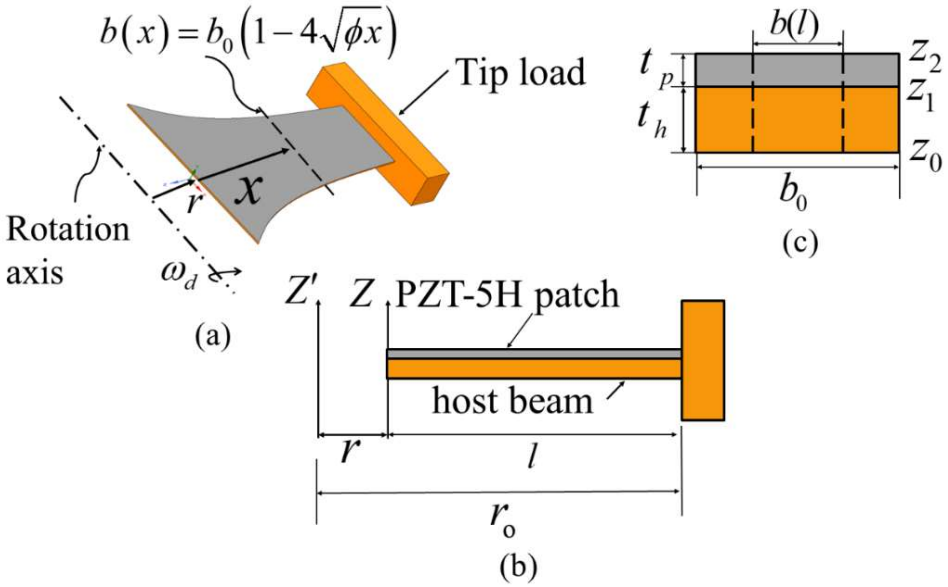

Figure 4.1 Schematics of the proposed parabolic varying cross-section piezoelectric harvester with tip load. The system is rotating about Y'-axis (a) Isometric view, (b) front view, and (c) left-hand side view

4.2.2 Electromechanical constitutive relations

The piezoelectric constitutive equations under the outline of Euler-Bernoulli theory, considering the host beam material as isotropic and homogeneous and using the tensor notations, can be given as;

$$\begin{aligned}\sigma_1 &= Y_{11}^E s_1 - e_{31} E_3 \\ D_3 &= e_{31} s_1 + \varepsilon_{33}^S E_3\end{aligned} \tag{4.1}$$

The displacement-strain relation considering a small transverse displacement along *Z*-direction and equivalent for every point on a cross-section is given as;

$$s_1 = -z\left[\frac{\partial^2 w(x,t)}{\partial x^2}\right] \tag{4.2}$$

To obtain the frequency responses and the motion equations, the total kinetic energy, potential energy, and the external work done of the tapered RVEH with tip mass is expressed utilizing Equations (4.1) and (4.2)(Chand et al., 2019a; Chand et al., 2019b; Salmani et al., 2015), as given below.

The total kinetic energy of the RVEH is the combination of the PZT-coupled structure and the tip load's kinetic energies, expressed as;

$$\begin{aligned}T_E = \frac{1}{2}\int_0^l \left\{\left[\rho_h A_h(x) + \rho_p A_p(x)\right]\left[\left(\frac{\partial w}{\partial t}\right)^2 + \omega_d^2 w^2\right]\right\} dx + M_L \omega_d^2 \left(\frac{\partial w}{\partial t}\right)^2_{x=l} \\ + \frac{1}{2} I_L \left[\left(\frac{\partial w}{\partial t \partial x}\right)_{x=l} + \omega_d\right]^2\end{aligned} \tag{4.3}$$

The total potential energy of the RVEH is expressed as;

$$U_E = \frac{1}{2}\int_{V_h} \sigma_1 s_1 dV_h + \frac{1}{2}\int_{V_p} \sigma_1 s_1 dV_p - \frac{1}{2}\int_{V_p} D_3 E_3 dV_p$$

$$= \frac{1}{2}\left\{ \begin{array}{l} \int_0^l \left[E_h I_h(x) + E_p I_p(x) \right] \left(\frac{\partial^2 w}{\partial x^2} \right)^2 dx \\ -\frac{2e_{31}}{t_p}\int_0^l J_p(x) v(t) \left(\frac{\partial^2 w}{\partial x^2} \right) dx - \frac{\varepsilon_{33}^S}{t_p}\int_0^l b(x) v^2(t) dx \end{array} \right\} \tag{4.4}$$

The voltage across the piezoelectric patch is related to the electric field along the *Z*-axis as;

$$v(t) = -E_3 t_p \tag{4.5}$$

In practice, to stimulate the vibration of the RVEH, the gravitational force in the system can be the driving force with a frequency equivalent to the rotational frequency. The component of the gravitational force (perpendicular to *X*-*Y* plane) on the total mass of the system to actuate the vibration is expressed as;

$$F_d(t) = Mg\sin(\omega_d t) \tag{4.6}$$

The total external workdone comprises the work done due to the resultant centrifugal forces of the rotating beam and the tip mass, the applied force to stimulate the vibration and the charge accumulated at the electrodes. The total external work done is given as;

$$W_E = \left\{ \begin{array}{l} \frac{1}{2}\int_0^l \left[A_h(x)\rho_h + A_p(x)\rho_p \right] \omega_d^2 (r) \left(\frac{\partial w}{\partial x} \right)^2 dx \\ +M_L (r+l)\omega_d^2 w_{x=l} + \frac{1}{2}\int_0^l F_d(t) \left(\frac{\partial w}{\partial x} \right)^2 dx \end{array} \right\} - Qv(t) \tag{4.7}$$

4.2.3 Discretization principle and equation of motion

The total kinetic energies, potential energies, and workdone are discretized using Galerkin's discretization approach. The transverse displacement is supposed to be a combination of spatial function and temporal coordinates, expressed as;

$$w(x,t)=\sum_{i=1}^{n}\boldsymbol{\psi}_i(x)\mathbf{u}_i(t) \tag{4.8}$$

The rotating tapered beam's normalized admissible function is considered as;

$$\psi_i(x)=(i+2)(i+3)x^{(i+1)}-2i(i+3)x^{(i+2)}+i(i+1)x^{(i+3)} \tag{4.9}$$

and

$$\boldsymbol{\Psi}=\{\psi_1,\psi_2,...,\psi_n\}\text{ and }\mathbf{u}=\{u_1,u_2,...,u_n\}^T \tag{4.10}$$

Now substituting Equation (4.8) in Equations (4.3), (4.4), and (4.7), we get,

$$T_E=\frac{1}{2}\begin{Bmatrix}\int_0^l\left(\left[\rho_hA_h(x)+\rho_pA_p(x)\right]\left\{\left[\sum_{i=1}^{n}\psi_i(x)\ddot{u}_i(t)\right]^2+\omega_d^2\left[\sum_{i=1}^{n}\psi_i(x)u_i(t)\right]^2\right\}\right)dx\\ +M_L\omega_d^2\left[\sum_{i=1}^{n}\psi_i(l)\ddot{u}_i(t)\right]^2+I_L\left\{\left[\sum_{i=1}^{n}\psi_i'(l)\dot{u}_i(t)\right]+\omega_d\right\}^2\end{Bmatrix} \tag{4.11}$$

$$U_E=\frac{1}{2}\begin{Bmatrix}\int_0^l\left[E_hI_h(x)+E_pI_p(x)\right]\left[\sum_{i=1}^{n}\psi_i''(x)u_i(t)\right]^2dx-\frac{\varepsilon_{33}^S}{t_p}\int_0^l b(x)v^2(t)dx\\ -\frac{2e_{31}}{t_p}\int_0^l J_p(x)v(t)\left[\sum_{i=1}^{n}\psi_i''(x)u_i(t)\right]dx\end{Bmatrix} \tag{4.12}$$

$$W_E=\frac{1}{2}\begin{Bmatrix}\int_0^l\left[A_h(x)\rho_h+A_p(x)\rho_p\right]\left(\omega_d{}^2r\right)\left[\sum_{i=1}^{n}\psi_i(x)u_i(t)\right]^2dx\\ +2M_L(r+l)\omega_d^2\left[\sum_{i=1}^{n}\psi_i(l)u_i(t)\right]+\int_0^l F_d(t)\left[\sum_{i=1}^{n}\psi_i(x)u_i(t)\right]^2dx-2Qv(t)\end{Bmatrix} \tag{4.13}$$

The Equations (4.11) – (4.13) can be expressed in terms of displacement coordinates, $\mathbf{u}=\{u_1,u_2,...,u_n\}^T$ as follows;

$$T_E=\frac{1}{2}\{\dot{\mathbf{u}}\}^T[\mathbf{M}]\{\dot{\mathbf{u}}\} \tag{4.14}$$

$$U_E=\frac{1}{2}\{\mathbf{u}\}^T[\mathbf{K}_U]\{\mathbf{u}\}+\{\mathbf{u}\}^T[\boldsymbol{\Delta}]\{\mathbf{u}\}-\frac{\varepsilon_{33}^S}{2t_p}\int_0^l b(x)v^2(t)dx \tag{4.15}$$

$$W_E=\frac{1}{2}\{\mathbf{u}\}^T[\mathbf{K}_C]\{\mathbf{u}\}+\frac{1}{2}\{\mathbf{u}\}^T F_d(t)[\mathbf{F}]\{\mathbf{u}\}-Qv(t) \tag{4.16}$$

In the above expressions, the matrices $[\mathbf{M}],[\mathbf{K}_U],[\boldsymbol{\Delta}],[\mathbf{K}_C]$ and $[\mathbf{F}]$ are defined as;

$$[\mathbf{M}]=\begin{Bmatrix}\int_0^l \rho_h t_h b(x)\left(\boldsymbol{\psi}(x)\right)^T\boldsymbol{\psi}(x)dx+\int_0^l \rho_p t_p b(x)\left(\boldsymbol{\psi}(x)\right)^T\boldsymbol{\psi}(x)dx\\ +\int_0^l \rho_h t_h b(x)\omega_d{}^2\left(\boldsymbol{\psi}(x)\right)^T dx+\int_0^l \rho_p t_p b(x)\omega_d{}^2\left(\boldsymbol{\psi}(x)\right)^T dx\\ +M_L\omega_d{}^2\left(\boldsymbol{\psi}(l)\right)^T\boldsymbol{\psi}(l)+I_L\left[\left(\boldsymbol{\psi}'(l)\right)^T\boldsymbol{\psi}'(l)+\omega_d{}^2\right]\end{Bmatrix} \tag{4.17}$$

$$\begin{aligned}[\mathbf{K}_U]=&\int_0^l E_h I_h(x)\left(\boldsymbol{\psi}''(x)\right)^T\boldsymbol{\psi}''(x)dx\\ &+\int_0^l E_p I_p(x)\left(\boldsymbol{\psi}''(x)\right)^T\boldsymbol{\psi}''(x)dx+M_L g\left(\boldsymbol{\psi}(l)\right)^T\end{aligned} \tag{4.18}$$

$$[\boldsymbol{\Delta}]=\frac{e_{31}}{t_p}\int_0^l b(x)I_p(x)\left(\boldsymbol{\psi}''(x)\right)^T dx \tag{4.19}$$

$$[\mathbf{K}_C]=\begin{Bmatrix}\int_0^l \rho_h r\omega_d{}^2 A_h(x)\left(\boldsymbol{\psi}'(x)\right)^T\boldsymbol{\psi}'(x)dx+\int_0^l \rho_p r\omega_d{}^2 A_p(x)\left(\boldsymbol{\psi}'(x)\right)^T\boldsymbol{\psi}'(x)dx\\ +2M_L(r+l)\omega_d{}^2\left(\boldsymbol{\psi}(l)\right)^T\end{Bmatrix} \tag{4.20}$$

$$[\mathbf{F}]=\int_{o}^{l}\left(\boldsymbol{\psi}'(x)\right)^{T}\boldsymbol{\psi}'(x)dx \tag{4.21}$$

Hamilton's equation is used to acquire the system's motion equations as;

$$\int_{t_1}^{t_2}\delta\left(T_E-U_E+W_E\right)dt=0 \tag{4.22}$$

Substituting Equations (4.14) – (4.16) in the Equation (4.22) and considering Ohm's law, the electromechanically coupled governing equations of motion for the rotating, PZT-coupled tapered RVEH in matrix form is obtained as;

$$\begin{aligned}&[\mathbf{M}]\{\ddot{\mathbf{u}}\}+[\mathbf{K}]\{\mathbf{u}\}-\{F_d(t)[\mathbf{F}]\}\{\mathbf{u}\}-[\boldsymbol{\Delta}]v(t)=0,\\&[\boldsymbol{\Delta}]^{T}\{\mathbf{u}\}+C_P v(t)-Q=0,\\&\frac{\partial Q}{\partial t}=-\frac{v(t)}{R}\end{aligned} \tag{4.23}$$

where, $[\mathbf{K}]=[\mathbf{K}_U]+[\mathbf{K}_C]$ and the capacitance $C_p=\int_0^l\left(l\varepsilon_{33}^{S}/t_p\right)b(x)\,dx$.

Internal structural damping in the form of classical Rayleigh damping(Wang et al., 2020) is considered for the system and introduced to the motion equations as damping matrix $[\mathbf{C}]$, i.e.,

$$[\mathbf{C}]=\gamma[\mathbf{M}]+\upsilon[\mathbf{K}] \tag{4.24}$$

where, γ and υ are proportionality constants.

The motion equations, considering the damping matrix, can be expressed as;

$$\begin{aligned}
&[\mathbf{M}]\{\ddot{\mathbf{u}}\}+[\mathbf{C}]\{\dot{\mathbf{u}}\}+[\mathbf{K}]\{\mathbf{u}\}-\{Mg\sin(\omega_d t)[\mathbf{F}]\}\{\mathbf{u}\}-[\boldsymbol{\Delta}]v(t)=0,\\
&[\boldsymbol{\Delta}]^T\{\mathbf{u}\}+C_P v(t)-Q=0,\\
&\frac{\partial Q}{\partial t}=-\frac{v(t)}{R}
\end{aligned} \tag{4.25}$$

The first part of Equation (4.25) is the general Mathieu-Hill equation with a periodic coefficient for the proposed tapered RVEHs with an internal structural damping effect. The RVEHs' natural frequencies are the real part of the square root of eigenvalues of the matrix $[\mathbf{M}]^{-1}[\mathbf{K}]$, which is equivalent to $[\boldsymbol{\omega}_n^2]$. Utilizing the Equations (4.17) – (4.21), (4.24), and (4.25), a MATLAB code is written to acquire the mechanical and electrical responses numerically.

4.3 Model Validation

Prior to estimating the RVEHs' performance and investigate the effects of the characteristic parameters, the proposed mathematical model is validated through FE simulation in ANSYS Mechanical APDL and experimental methods. The proposed model is also validated against earlier reported rectangular RVEH. This is accomplished by using $\phi=0$ in the present formulation which convert the RVEHs into rectangular one.

4.3.1 Validation through FE simulation

For the validation purpose, a system, with r = 7.5 mm, ϕ= 0.4, M_{LM} =15.1808 gram, and the dimensions given in Table 3.2, has been considered. The physical properties of PZT-5H are provided in Table 1.1.

The finite element (FE) simulation of the proposed parabolic tapered RVEH is conducted in ANSYS Mechanical APDL 18.0. The FE layout of the system with a parabolic tapered harvesting beam and a tip-load is shown in Figure 4.2. The parabolic curves' x, y, and z coordinates are obtained using the width variation function (over 200 keypoints for both sides) and connected through spline. The various element types used for the different RVEH components are given in Table 4.1. An Electroelast/Piezoelectric Coupled-field element is used to discretize the model with a tetrahedral mesh. The Circuit 94 element type is used to define the resistance between the two electrodes. A smart finer mesh is applied, resulting in the creation of almost 20000 elements. The voltage coupling is used to simulate the electrodes on the PZT 5H surfaces. The voltage coupling is represented by the VOLT and CP in Figure 4.3. All the nodes on the top surface of the PZT patch are assignrd 0 V, which acts as ground. In the simulation, rotational frequency is applied about the *Y*-axis as the angular velocity. Then simulations are conducted to obtain the peak output voltage of the RVEH for a driving frequency range of 0.7-20 Hz.

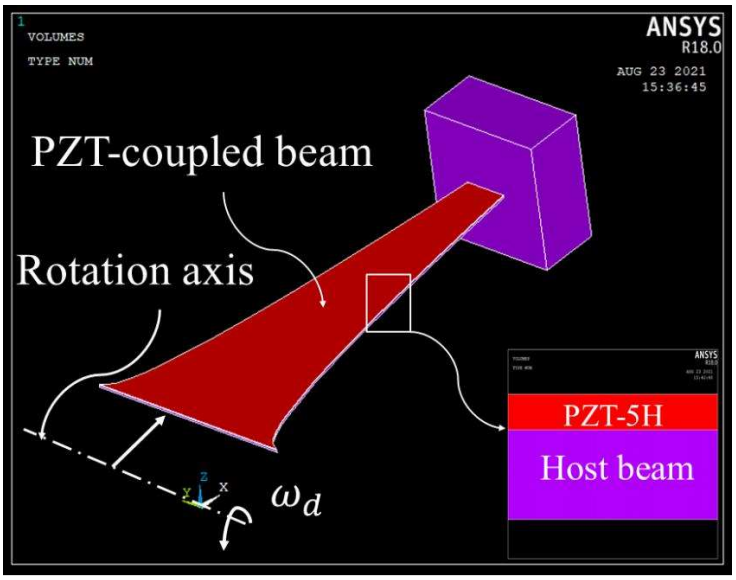

Figure 4.2 The FE layout of the proposed parabolic tapered RVEH's components and the thicknesses of the PZT-coupled beam

Table 4.1 The element types used for various components of the RVEH

Components	Element type
PZT-5H	Electroelast/Piezoelectric Coupled-field tetrahedral (SOLID227)
Brass host	Plane SOLID227
Tip load	Plane 285
Resistive load	CIRCU94

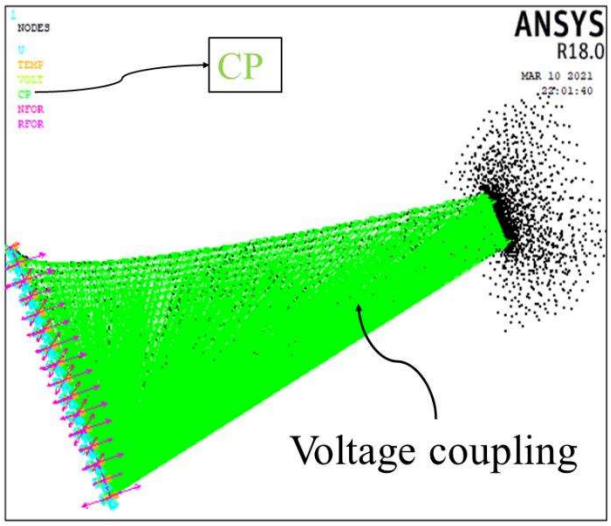

Figure 4.3 The voltage coupling to simulate the electrodes over the PZT surfaces

A similar FE simulation procedure as discussed earlier is followed for the exponentially tapered RVEH. In this case, similar material properties, dimensions, and element types are considered except l = 62 mm, ϕ =10, and M_{LM} = 46.3 gram as shown in Figure 4.4. Here the tip load mass is intentionally increased to bring the harvester's natural frequency to lower values to conduct a parametric analysis for self-frequency-tuning purpose.

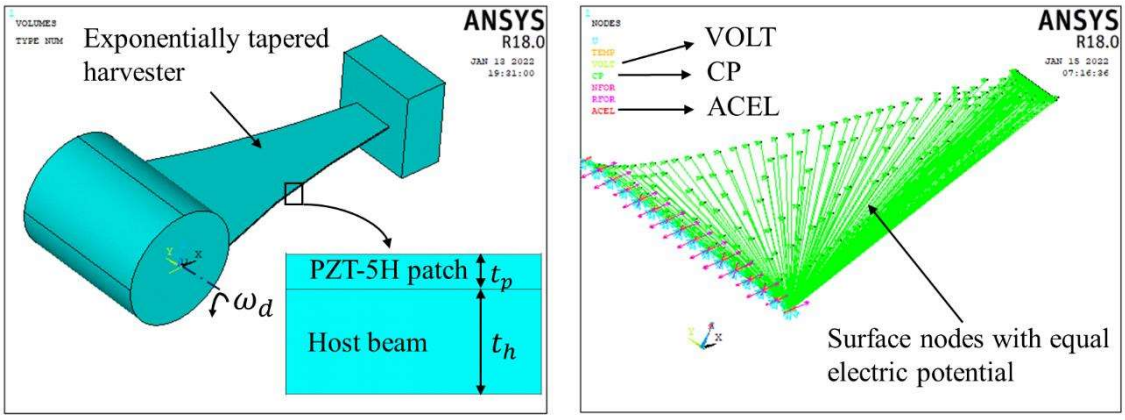

Figure 4.4 The FE model of the proposed exponentially tapered RVEH (a) The components of the RVEH and the thicknesses of the PZT-coupled beam (b) Voltage coupling used to replicate the electrodes on the PZT-surfaces

4.3.2 Validation through experimental methods

In order to validate the proposed formulations, an experiment is set up using a parabolic tapered RVEH. For this purpose, a system with ϕ = 0.4, M_{LM} =15.1808 gram, and the dimensions of the host beam and PZT-5H given in Table 3.2 are considered. The details of prototype fabrication, setup construction, and experimental method for parabolic and exponentially tapered RVEH are given in Appendix IV. In the proposed numerical model, the Rayleigh damping coefficients are chosen as γ = 7 s^{-1} and υ = 2 x10^{-6} s for the parabolic tapered beam and γ = 1 s^{-1} and υ = 6 x10^{-6} s for the exponentially tapered beam. Relative errors between the experimental and numerical output voltage are within 20%, which is acceptable(Wang et al., 2020). After that, the experiments were conducted for the rotational frequency range of 0.7 Hz- 20 Hz. The numerical solution and FE simulations are likewise carried out using the identical parameters and rotational frequencies as those used in the experiments.

The experimental, numerical, and FE results of the parabolic tapering RVEH are presented in Figure 4.5. It can be observed that the OC response of the harvester improves as the driving frequency increases. It can be noticed that the theoretical responses are similar to the experimental ones at low-frequency regions, which validate the proposed mathematical formulations. The substantial difference between the experimental and theoretical responses is because of the appearance of nonlinearities associated with geometry and material at higher driving frequency. The discrepancy between the numerical and experimental response at 10.08 Hz is found to be 12.92 %, whereas, at 20.2 Hz, it is determined to be 39.5%. Therefore, a frequency range of 0.7-12.2 Hz is considered in this paper for the parametric analysis. From the experimental

analysis, the generated peak open-circuit voltage at 0.71 Hz is found to be 252 mV from the considered prototype.

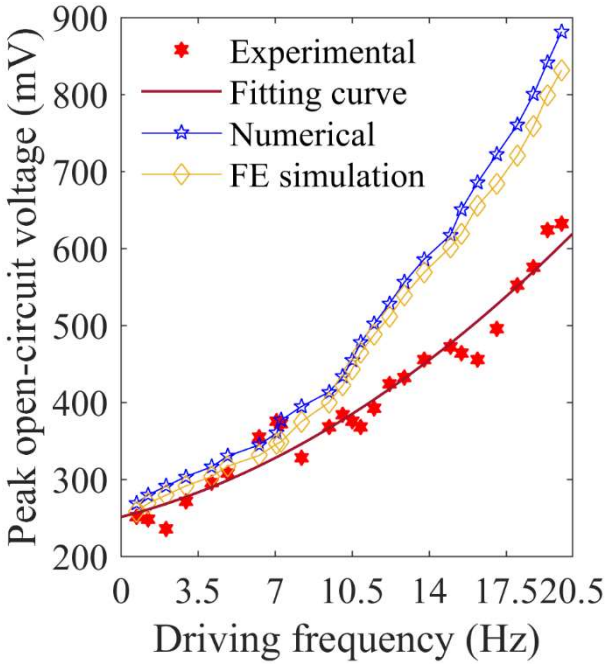

Figure 4.5 The peak OC voltage response of the parabolic tapering width RVEH against driving frequency

In experimental validation of the exponentially tapered RVEH the tip load mass is increased to 46.3 grams. This increase in the tip load increases the OC voltage response of the RVEH while moving the resonance frequency to lower values. Although the output voltage from the harvester rises with the increase in the tip load, the VPM of the harvester is not essentially increased as the mass of the system simultaneously increases with an increase in generated voltage. The experiments were conducted for the rotational frequency range of 0.7 Hz- 10 Hz. The numerical solution and FE simulations are carried out using the identical parameters and rotational frequencies as those used in the experiments. The experimental, numerical, and FE results of the exponentially tapering RVEH are presented in Figure 4.6. The maximum output OC voltage from the

numerical, FE and experimental methods are found to be 2.596 V, 2.632 V, and 2.575 V, respectively. The corresponding natural frequencies are 6.75 Hz, 6.80 Hz, and 6.65 Hz, respectively. It can be noticed that the theoretical responses are similar to the experimental ones, which validate the proposed mathematical formulations.

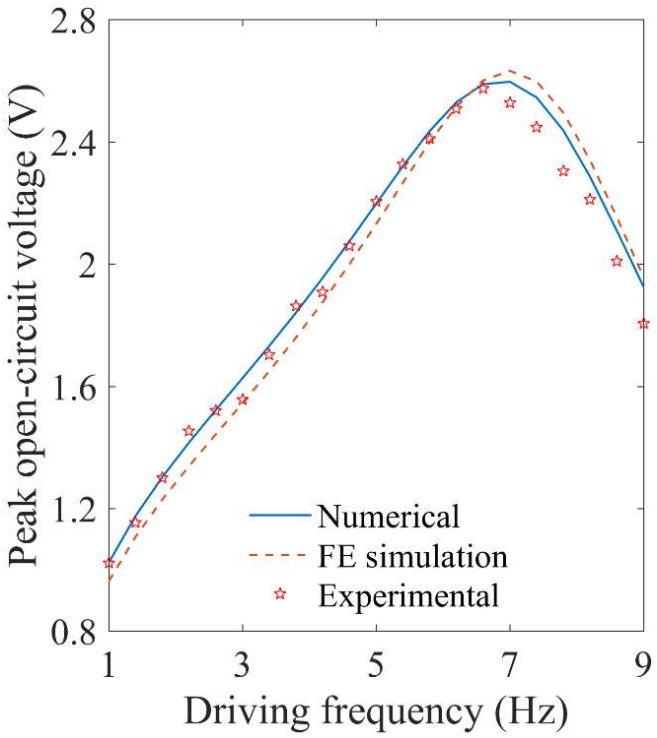

Figure 4.6 The peak open-circuit voltage response of the exponentially tapered RVEH against driving frequency

4.3.3 Validation through earlier numerical models

Moreover, the present model is verified against the past reported rectangular harvesters. The comparison is accomplished by taking $\phi = 0$ in the current formulation, which converts the present formulations into a formulation of a rectangular harvester. The comparison is given in Table 4.2. The VR represents the reported output voltage, and VC represents the calculated output voltage using the current model. The close agreement between the reported and calculated results also verified the proposed model.

Table 4.2 Verification of the present model against the past reported rectangular harvesters

References	Harvester shape	Operating freq. (Hz)	VR (V)	VC (V)
Xie et al.(2018)	Rectangular	1–14	1.2–3	-
Khameneifar et al. (2013)	Rectangular	0–28.65	4.5/15	4.29/ 14.88
Guan and Liao (2016)	Rectangular	7–13.5	5–35	4.87–34.6
Gu and Livermore (2012)	Rectangular	4–16.2	0–5.5	5.38
Deng et al. (2020)	Trapezoidal	10–20	3–12.6	–
Present study	Parabolic	0.7–20.1	–	0.882
Present study	Exponential	0.7–10	–	2.575

4.4 Performance Comparison

From the experimental analysis, the generated peak open-circuit voltage of the parabolic tapering RVEH at 0.71 Hz is found to be 252 mV from the considered prototype. The harvester's voltage-per-total mass (VPM) and power density (PD) at 20.1 Hz driving frequency are found to be 30.88 V/Kg and 6.11 $\mu W/mm^3$, respectively. The VPM produced by the earlier reported models is calculated and compared with the current model and presented in Table 4.3.

From the experimental analysis of the exponentially tapering RVEH, the peak OC voltage and the VPM is found to be 2.575 V and 28.15 V/Kg at the rotational driving frequency of 6.65 Hz. The PD from the exponentially tapering harvester is found to be 5.27 $\mu W/mm^3$, as given in Table 4.3.

The VPM obtained from the present models is significant in comparison to the previously reported rotational harvesters. Table 4.3 also shows the performance amplification factor (PAF) of the considered harvesters to compare the tapering cross-section harvester's performance with their uniform counterpart.

Table 4.3 Performance comparison of the proposed parabolic and exponentially tapered RVEHs with some other reported models

References	Harvester shape	Piezo. material	Operating freq. (Hz)	VR (V)	VC (V)	PDR (μWmm^{-3})	PDC (μWmm^{-3})	VPM (V/Kg)	PAF
Salmani and Rahimi(2015)	Rectangular	PZT 5H	1–14	1.2–3	–	0.1	–	26.15	–
Baker et al.(2005)	Rectangular	PZT/PVDF	0–28.65	4.5/15	4.29/14.88	0.12/5.98	0.115/5.96	8.256	–
Dietl and Garcia(2010)	Rectangular	PSI-5A4E	7–13.5	5–35	4.87–34.6	1.01	0.989	11.146	–
Paquin and Amant (2010)	Rectangular	PVDF	4–16.2	0–5.5	5.38	0.031	0.03	18.724	–
Keshmiri and Wu(2018)	Trapezoidal	PZT 4	10–20	3–12.6	–	2.94	–	17.522	2.89
Present study	Parabolic	PZT 5H	0.7–20.1	–	0.882	–	6.11	30.88	4.18
Present study	Exponential	PZT 5H	0.7–10	–	2.575	–	5.27	28.15	3.14

4.5 Summary

This chapter presents the electromechanical coupled mathematical modeling of the proposed parabolic and exponentially tapered RVEH. The multimodal coupled motion equations in the framework of Euler-Bernoulli beam theory are obtained using Hamilton's principle and Ohm's law. Galerkin's discretization approach is used for the approximate solutions. After that, the proposed model is verified using FE simulations in ANSYS Mechanical APDL, and an experiment is set up to validate the proposed numerical model. Finally, the PD and VPM of the proposed RVEHs are calculated to compare with the earlier reported models.

From the experimental analysis, the generated peak OC voltage of the parabolic tapering RVEH at 0.71 Hz is 252 mV from the considered prototype. The harvester's VPM and PD at 20.1 Hz driving frequency are 30.88 V/Kg and 6.11 $\mu W/mm^3$, respectively. The exponentially tapering RVEH shows the peak OC voltage, VPM, and PD are 2.575 V, 28.15 V/Kg, and 5.27 $\mu W/mm^3$ at the rotational driving frequency of 6.65 Hz. Compared to earlier reported models, these are significant advantages.

In conclusion, the numerical model proposed in this chapter is valid up to 12 Hz driving frequency, which corresponds to the rotational speed of 720 RPM. The 12 Hz driving frequency range is enough for designing any rotational vibration energy harvester. At higher excitations, the experimental results deviate from the numerical results because of the nonlinearity. Increasing the tip load moves the resonance frequency to lower frequencies and increases the voltage output from the RVEH.